Article

Monitoring Electron–Phonon Interactions in Lead-Halide Perovskites Using Time-Resolved THz Spectroscopy

Daming Zhao, Hongwei Hu, Reinhard Haselsberger, Rudolph A Marcus, Maria-Elisabeth Michel-Beyerle, Yeng Ming Lam, Jian-Xin Zhu, Chan La-o-vorakiat, Matthew C. Beard, and Elbert E. M. Chia

ACS Nano, **Just Accepted Manuscript** • DOI: 10.1021/acsnano.9b02049 • Publication Date (Web): 26 Jul 2019

Monitoring Electron–Phonon Interactions in Lead-Halide Perovskites Using Time-Resolved THz Spectroscopy

Daming Zhao,[†] Hongwei Hu,[‡] Reinhard Haselsberger,[†] Rudolph A. Marcus,[†] Maria-Elisabeth Michel-Beyerle,[†] Yeng Ming Lam,[‡] Jian-Xin Zhu,[§] Chan La-o-vorakiat,[*,∥] Matthew C. Beard,[*,#] and Elbert E. M. Chia[*,†]

†*Division of Physics and Applied Physics, School of Physical and Mathematical Sciences, Nanyang Technological University, 637371, Singapore*

‡*School of Materials Science and Engineering, Nanyang Technological University, 639798, Singapore*

¶*Noyes Laboratory, California Institute of Technology, Pasadena, California 91125, USA*

§*Theoretical Division and Center for Integrated Nanotechnologies, Los Alamos National Laboratory, Los Alamos, New Mexico 87545, USA*

∥*Nanoscience and Nanotechnology Graduate Program, Faculty of Science, King Mongkut's University of Technology Thonburi (KMUTT), 10140 Thailand*

⊥*Theoretical and Computational Science Center (TaCS), KMUTT, Bangkok 10140 Thailand*

#*Chemistry and Nanoscience Science Center, National Renewable Energy Laboratory, Golden, Colorado 80401, USA*

E-mail: chan.laovorakiat@gmail.com; Matt.Beard@nrel.gov; elbertchia@ntu.edu.sg

Abstract

Lead-halide perovskite semiconductors have low-frequency phonon modes within the lead-halide sublattice and thus are considered to be soft. The soft lattice is considered to be important in defining their interesting opto-electronic properties. Electron–phonon coupling governs hot-carrier relaxation, carrier mobilities, carrier lifetimes, among other important electronic characteristics. Directly observing the interplay between free-charge carriers and phonons can provide details on how phonons impact these properties, *e.g.* exciton populations and other collective modes. Here, we observe a delicate interplay among carriers, phonons and excitons in mixed-cation and mixed-halide perovskite films by simultaneously resolving the contribution of charge carriers and phonons in the time-resolved terahertz photoconductivity spectra. We are able to observe directly the increase in phonon population during carrier cooling and discuss how thermal equilibrium populations of carriers and phonons modulate the carrier transport properties, as well as reduce the population of carriers within band tails. We are also able to observe directly the formation of free-charge carriers when excitons interact with phonons and dissociate, and to describe how free carriers and exciton populations exchange through phonon interactions. Finally, we also time-resolve how the carriers are screened *via* the Coulomb interaction at low and room temperatures. Our studies shed light on how charge carriers interact with the low-energy phonons and discuss implications.

Keywords

perovskite, time-resolved terahertz spectroscopy, phonon, free carrier, exciton

The combination of excellent photovoltaic performance and solution processability has brought organic-inorganic hybrid perovskites into the forefront of solar cell research.[1] The collusion of favorable properties, such as strong and broadband visible light absorption,[2] long ($\sim$1 μm) and balanced electron and hole diffusion lengths,[3,4] ensures that upon solar illumination, electron–hole pairs can form, dissociate, and quickly drift away from the active regions and towards the electrodes before loss processes such as recombination occur.

The most studied lead-halide perovskite is methylammonium lead iodide ($MAPbI_3$).[4–7] However, $MAPbI_3$ suffers from stability issues, *e.g.* degradation by ultraviolet light and moisture in air.[8,9] By mixing the inorganic cesium cation in both $MAPbX_3$ (X = Cl, Br or I) and $HC(NH_2)_2PbX_3$ ($FAPbX_3$), the stability can be greatly improved.[10,11] In addition, the band gap becomes tunable from 1.73 eV to 1.48 eV by increasing the size of the cation from Cs to MA to FA, and from 1.48 eV to 2.23 eV by mixing bromine and iodine halides.[12] One of the highest power conversion efficiencies (PCEs) of 22.1%[13] is obtained from solar cells based on mixed-cation and mixed-halide systems. We therefore focus our study on these mixed-cation and mixed-halide systems rather than the canonical $MAPbI_3$.

In our work we capture both free-carrier and the low-frequency phonon dynamics by utilizing a broadband terahertz (THz) probe pulse. In the THz frequency range (1 THz = 4.1 meV), free carriers readily absorb the THz light with an absorption cross section that is proportional to the carrier mobility through a Drude-type mechanism.[14] Within the same THz frequency range are the resonance frequencies of the lowest-lying optical-phonon modes. These phonon modes originate from vibrations of the metal-halide sublattice.[15–17] In fact, one of the features of Pb-halide perovskites that distinguishes them from traditional semiconductors is that optical phonon modes are low in energy, indicating a soft lattice with easily polarizable bonds. Here we take advantage of the spectral overlap of energies to study the carrier population number and the phonon dynamics simultaneously, giving great insight to carrier–phonon interactions. That is, time-resolved THz spectroscopy (TRTS) is able to monitor the photoinduced carrier dynamics and carrier-induced changes in phonon modes,

simultaneously. Moreover, frequency-resolved TRTS extracts both the real and imaginary parts of the photoinduced change in the complex optical conductivity (or photoconductivity), without the need to invoke Kramers-Kronig transformation. Knowledge of both the real and imaginary parts of the dielectric function restricts the physical models that can explain the data, which is crucial for subsequent data interpretation.

Previous studies have shown that the frequency-resolved TRTS data exhibit features near the phonon mode frequencies. However, care must be taken to avoid data analysis artifacts.[18] Moreover, those studies attributed these features to carrier–phonon coupling without a suitable model[19,20] that can adequately describe their data. Furthermore, those studies only focus on carrier recombination and track only the long-time dynamics after $\sim$5 ps, missing out on earlier-time dynamics such as carrier cooling.

For the mixed-cation mixed-halide perovskite films studied in this paper, our analysis of dynamics from 0.4 ps to 3000 ps, at both low and room temperatures, reveal a significant change in the phonon mode profile and carrier–phonon scattering channels during carrier relaxation (earlier than 10 ps). Analysis of the carrier and phonon spectral weights reveal correlations between them, that suggest the intricate interplay among phonon emission during carrier relaxation, exciton dissociation *via* phonon absorption, and photoenhanced carrier screening, that cooperatively ensures a large and long-lived carrier population. Though one can observe carrier relaxation from transient absorption spectroscopy,[21,22] or deduce carrier–phonon coupling from photoluminescence measurements,[23] in our experiments we are able to, within the same set of data, explain the dynamics of carriers, excitons and phonons, and their mutual interplay, all within one self-consistent picture.

Results and Discussion

Extraction of phonon and carrier contribution

We begin our investigation of $FA_{0.85}Cs_{0.15}Pb(I_{0.97}Br_{0.03})_3$ thin film (FCPIB) by measuring the equilibrium (*i.e.* without pump, or dark) complex optical conductivity $\tilde{\sigma}(\omega) = \sigma_1(\omega) + i\sigma_2(\omega)$ at 15 K, as shown in Fig. 1B. We observe peaks at 0.85 THz ($\hbar\omega_{TO,1} = 3.6$ meV) and 1.80 THz ($\hbar\omega_{TO,2} = 7.4$ meV) that originate from transverse-optical (TO) phonon absorption (labeled as mode 1 and 2, respectively). They correspond to a series of TO phonon-modes related to the vibrations of Pb–halide bonds.[16,17] Their conductivity can be described by a Lorentzian profile.[14,24] We performed a loss function analysis[17,25,26] (Supplementary Fig. S1B) and found the longitudinal-optical (LO) phonon modes to be located at higher energies of 1.15 THz ($\hbar\omega_{LO,1} = 4.8$ meV) and 3.57 THz ($\hbar\omega_{LO,2} = 14.8$ meV).

Next, we excite FCPIB with 60-fs, 37 μJ/cm^2 laser pulses with a photon energy of 1.57 $\pm$ 0.02 eV. In this work, all TRTS measurements were performed under the same excitation conditions. The photon energy is close to the bandgap energy of $\sim$ 1.57 eV (Supplementary Fig. S4), which has just enough energy to create excitons and electron–hole plasma with very little excess energy, and avoids complex scenarios such as hot-carrier injection or multiple valley excitations. We then vary the optical path difference to scan the time delay τ between the optical pump pulse and THz probe pulse, to obtain a full two-dimensional frequency-resolved THz spectra of FCPIB photoconductivities (Fig. 1C,D) (see Methods Section).

Our frequency-resolved photoconductivities do not display solely a Drude-like characteristic as is expected for photogenerated free charge carriers, but rather they also contain a derivative-like profile located near the two phonon peaks determined from our dark measurements. Such features have been reported on other perovskite semiconductors, either as a dip in the transmission spectra of $MAPbI_{3-x}Cl_x$[19] or an asymmetric photoinduced phonon profile in the photoconductivity spectra of $MAPbI_3$.[6] These features were attributed to the presence of carrier–phonon coupling, though the asymmetry seen here in FCPIB is more

pronounced. The photoconductivity can be quantitatively described by a combination of Drude-Smith (DS) and Peak-Shift (PS) contributions (see Supporting Information, Section S10 for more details):

$$\Delta\tilde{\sigma}(\omega,\tau) = \Delta\tilde{\sigma}_{DS} + \Delta\tilde{\sigma}_{PS},$$

where the DS term is conventionally used to account for the presence of free charge carriers inside a disordered environment.[27,28] From the DS contribution to the overall response we can determine the carrier density and the carrier scattering rate. We introduce the PS term that accounts for a change in the phonon profile in the presence of free carriers. Both the resonant frequency and oscillator strength of the phonon modes are modified, and the PS term has a mathematical form that is related to the derivative of the Lorentzian function. We attribute this change in the phonon profile to the combined effects of phonon anharmonicity (predicted by density-functional theory in $MAPbI_3$)[29] and large ionic displacements upon photoexcitation (from ultrafast electron diffraction data)[7] (see Supporting Information, Section S8 for more discussions).

From using a non-linear least-squares fitting routine to find best-fit parameters that describe our observed data, we extract the photogenerated free charge carrier density (*via* the Drude plasma frequency), carrier scattering rate (*via* the Drude scattering rate) and the modulation of phonon profiles (*via* the PS terms).

Carrier–phonon scattering channels: physical model and experimental data

Before we discuss the best-fit parameters, we first introduce the carrier relaxation scheme that we deduced from our data (Fig. 2A,B).[30] For simplification, we only describe the relaxation from the perspective of electrons, as holes are expected to behave similarly due to their roughly equal effective masses.[31]

Immediately after photoexcitation, electrons thermalize within 100 fs.[21,22] Electrons pos-

sess energies (in excess of the bandgap) above the two lowest-lying LO-phonon modes. Carrier relaxation is dominated by carrier–LO-phonon interactions *via* the Fröhlich mechanism. The energies of the two LO-phonon modes motivate us to partition the electron relaxation process into three regions *i*, *ii*, *iii*, as shown in Fig. 2A. In region *i*, where the electron energy E is larger than that of the two LO-phonon modes ($E > \hbar\omega_{LO,2} > \hbar\omega_{LO,1}$), electrons can interact with the two phonon modes *via* four scattering channels — phonon absorption and emission from both modes 1 and 2.

The electrons then lose energy and enter region *ii*, where $\hbar\omega_{LO,2} > E > \hbar\omega_{LO,1}$. Here, the electrons do not have enough energy to participate in the carrier–phonon scattering process that involves the emission of $\hbar\omega_{LO,2}$-phonons, so there are now only three energetically-permissible scattering channels. Similarly, as the electrons relax close to the conduction band minimum in region *iii* ($\hbar\omega_{LO,2} > \hbar\omega_{LO,1} > E$), they cannot emit either $\hbar\omega_{LO,1}$- or $\hbar\omega_{LO,2}$-phonons, and we are left with only two scattering channels of phonon absorption. At the bottom of the band, carrier recombination across the bandgap dominates.

The above picture is strictly valid at 0 K. At finite temperatures, thermal broadening caused by the high-energy tail in the Fermi-Dirac distribution and hence state occupancy distribution (see Fig. 2C), results in transitions between the regions to be gradual rather than step-like. For example, inside region *ii*, even though the mean energy $\langle E \rangle$ of the electrons obey $\hbar\omega_{LO,2} > \langle E \rangle > \hbar\omega_{LO,1}$, a small fraction of the electrons can still be located in region *i*, which opens up all four scattering channels there. At room temperature, all four scattering channels open up at all time delays, enabling electron relaxation to take place simultaneously with carrier recombination. Thus, a thermal distribution of electrons, phonons and excitons are produced. Carriers interact strongly with phonons by continually losing and gaining energy to maintain the thermal distribution at room temperature. This is quite distinct from other typical semiconductors with larger LO-phonon mode energies than in the halide perovskites, where thermalized carriers cannot emit phonons, and the phonon population at room temperature is not so great such that carriers do not continually interact with a large

population of phonons. In our system the carriers are constantly emitting and absorbing phonons. Two main consequences arise from these interactions: (1) it limits the carrier mobility as the number of scattering channels is increased, and (2) it provides a pathway to detrap carriers from shallow band tails.

The experimental evidence of quasi-step-like reduction of scattering channels and our regional assignment of the conduction band are found in the measured carrier scattering rate extracted through Drude analysis (Fig. 2D,E), which is proportional to the number of scattering channels according to Matthiessen's rule.[32] At the low temperature of 15 K, where there is minimal thermal broadening, Figure 2D shows that the scattering rates at early (region *i*: $\tau < 0.6$ ps), intermediate (region *ii*: 1.2 ps $< \tau <$ 2.2 ps) and long (region *iii*: $\tau >$ 10 ps) time delays exist in the approximate ratio 3.8:2.9:2.0. This is close to the 4:3:2 ratio expected from the number of possible scattering channels in the three regions. Additional support for our interpretation is provided by data at higher temperatures (65 K $\approx$ 5.4 meV, and 285 K $\approx$ 24 meV) — see Fig. 2E. Due to thermal broadening at finite temperatures (see Fig. 2C), electrons can now populate region *i* (with four scattering channels) with finite probability, with two consequences: (1) the 65 K and 285 K scattering rates are similar to that of the 15 K data with four scattering channels, and (2) the change of scattering rate between regions is no longer observable. The fact that the four-channel scattering rate at 285 K is slightly higher than that at 65 K, which in turn is slightly larger than that at 15 K, is again a consequence of a longer Fermi-Dirac high-energy tail with increasing temperature.

It is interesting to note that the scattering rate at early times ($\tau \leq 1$ ps) for 65 K and 285 K is smaller than the long-delay-time values, *i.e.* showing fewer than four scattering channels. Since we are exciting our sample with 20-meV bandwidth photons centered at the band edge ($\sim$1.57 eV), a majority of the photoexcited carriers would have a kinetic energy of only 5–10 meV, *i.e.* $\sim$60–120 K. Thus, after about 100 fs, the thermalized carriers would have a lower temperature than the lattice at higher temperatures (*e.g.* 65 K and 285 K), and so would not have access to all four scattering channels. Subsequently, these carriers are

then “warmed up" by the lattice after a few hundred fs.

Note that scattering from acoustic phonons is significant only when the carriers have cooled to near the band edge, such that the carrier energy is smaller than the energy of both LO-phonon modes, *i.e.* region *iii* in our analysis.[30] In regions *i* and *ii*, the carrier relaxation time is dominated by interactions with LO phonons through the Fröhlich interaction. Hence, in our present work on a halide perovskite semiconductor, it is reasonable to consider only the carrier–LO-phonon interaction in our analysis and interpretation.

Here we are able to resolve directly the subtle role that phonons play in thermalized carrier distribution. The energies of the lowest-lying phonon modes, relative to the operation temperature, determine the number of carrier scattering channels and hence the scattering rate and carrier mobility of photogenerated free carriers. The carrier relaxation dynamics picture obtained in this section forms the basis of our subsequent analysis of carrier density and phonon spectral weights, which will be discussed in the following sections.

Disentanglement of carrier recombination and relaxation

Next we show that the phonons, *via* their emission by free carriers and/or absorption by excitons, directly affect the density of photogenerated carriers. We do this by monitoring two types of spectral weights: (1) Drude spectral weight, which is proportional to the square of the Drude plasma frequency (ω_{pD}^2), is a direct measure of the number density of photogenerated free charge carriers, $n = \epsilon_0 \omega_{pD}^2 m^{**}/e^2$, where $m^{**} = 0.24 m_0$ is the electron polaronic effective mass[31] (see Supporting Information, Section S3); (2) phonon spectral weight, proportional to ω_{pk}^2, and is a measure of the change in phonon oscillator strength induced by photoexcitation.

First we have to distinguish between carrier thermalization, carrier cooling (or carrier relaxation), and carrier recombination. Carrier thermalization is the process whereby the initially-excited carrier distribution by the laser pulse forms a thermal (Fermi-Dirac) distribution and is not studied here, but is dominated by electron–electron interactions and thus no energy is exchanged with the lattice. Carrier cooling is the process of electrons (holes)

cascading down (up) the conduction (valence) band minimum (maximum) that involves an exchange of energy (∼meV) with the lattice through phonons. Neither carrier thermalization nor carrier cooling changes the number of photogenerated electron–hole pairs, but their transport properties are modified. However, there is also an interaction among free charge carriers, phonons, and excitons. The formation of excitons through phonon emission (by free carriers) will decrease the free charge carrier population. Conversely, the dissociation of excitons *via* phonon absorption will increase the free charge carrier population. Finally, carrier recombination results in recombination of electron and holes and releases energy of the order of the bandgap (∼eV). Carrier recombination can occur through radiative processes where the energy is radiated back to the environment or non-radiative recombination where the energy is exchanged with the lattice. A very general description of carrier recombination obeys the rate equation

$$\frac{dn(\tau)}{d\tau} = -k_1 n - k_2 n^2 - k_3 n^3,$$

where the rate constants k_1, k_2 and k_3 describe (first-order) trap-state-mediated, (second-order) bimolecular, and (third-order) trimolecular recombinations, respectively.

Figure 3A shows that, at 15 K, $1/n^2$ is linear in from 10 ps to 600 ps, indicating that at these carrier densities, carrier recombination is predominantly third-order. The third-order process is usually assigned to an Auger recombination mechanism, where the energy required to recombine an electron–hole pair is provided by an intraband transition of a third charge carrier. A similar third-order recombination is also seen in $MAPbI_3$ with similar carrier density at the same temperature.[6] Figure 3B shows how ω_{pD}^2 (and photogenerated carrier density n) changes with pump-probe delay time τ. The fitting parameters, obtained from the weighted-least-squares linear fit in Fig. 3A from 10 – 600 ps, were used to plot the solid line in Fig. 3B, and then extrapolated down to 0.6 ps and up to 3000 ps. We find that the third-order recombination (solid-black trace) significantly underestimates the carrier density for delay times less than 10 ps, which interestingly was previously marked as the boundary between region *ii* and *iii* in Fig. 2D. As will be explained in the subsequent paragraphs, this

underestimation is primarily caused by the processes of phonon-assisted exciton dissociation and formation, that affects carrier density prior to 10 ps.

We now examine the correlation between the carrier and phonon dynamics below 10 ps. To isolate the change in carrier density due solely to phonon absorption/emission, we subtract the raw data in Fig. 3B by the third-order-recombination solid line, yielding the purple trace. Figure 3C displays the time evolution of the spectral weights of phonon modes 1 and 2. By comparing Fig. 3B and 3C, we see that in region *ii*, there is an anti-correlation between the carrier and phonon spectral weights — a decrease in phonon spectral weights (of both modes 1 and 2) is accompanied by an increase in the carrier spectral weight. The phonon dynamics in Fig. 3C agree with our proposed relaxation scheme in Fig. 2A, where no emission of high-energy $\hbar\omega_{LO,2}$-phonons is allowed in region *ii*.

In the transition region between *i* and *ii*, as mentioned earlier, the high-energy tail in the finite-energy Fermi-Dirac distribution implies a finite fraction of electrons with energies exceeding $\hbar\omega_{LO,2}$, which after relaxation, results in the emission of the higher-energy $\hbar\omega_{LO,2}$-phonons. Hence in this transition region, we see an increase in the spectral weight of phonon mode 2 as shown in Fig. 3C. Similarly, in the transition region between *ii* and *iii*, carriers do not have enough energy to emit the $\hbar\omega_{LO,2}$-phonons, and so there is only a very slow $\hbar\omega_{LO,2}$-absorption all the way through region *iii* (see long arrow in Fig. 3C). A slow emission of $\hbar\omega_{LO,1}$-phonons (by free carriers) can still take place (due to high-energy tail in the state occupancy above $\hbar\omega_{LO,1}$, shown in the inset of Fig. 3B), resulting in the formation of excitons.

The anti-correlation between the carrier and phonon spectral weights, seen in Figs. 3B and 3C, can be explained by the phonon-assisted exciton dissociation/formation. In the lead-halide perovskites, the exciton binding energies are reported to be $\sim$10 – 16 meV,[33,34] are in the same range as the LO-phonon mode energies. The excitons dissociate by absorbing LO-phonons, creating unbound (*i.e.* free) electrons and holes, resulting in an increase in carrier spectral weight and hence carrier density. These LO-phonons were provided by the relaxation of the photogenerated carriers as they relax towards the band edge (discussed in

the previous section). Since we pump the sample very close to the bandgap, optical excitation should provide just enough energy to create excitons, leading to the coupled dynamics among carriers, phonons and excitons *via* exciton–phonon coupling that was previously observed in 2D hybrid perovskites *via* temperature-dependent photoluminescence linewidth broadening.[35]

Figure 3D shows the coupled dynamics of carriers, excitons and phonons, with associated excitation spectrum of electron–hole pairs. Without excitons, phonon emission/absorption changes only the carrier energy, not density (red box). For the phonons to change the carrier density, they must be either absorbed by the excitons (causing exciton dissociation and increasing carrier density) or emitted by free carriers (causing exciton formation and decreasing carrier density) (see blue box).

We next wish to see if the anti-correlation between the carrier and phonon spectra weights, observed at 15 K, is still preserved at room temperature. Figure 4A shows the same anti-correlation occurring at 285 K, but now over a much longer timescale — the carrier spectral weight shows a slow but monotonic increase even up to 3 ns, with a concomitant slow and monotonic decrease in the phonon spectral weights (Fig. 4B) over the same timescale. Our room-temperature result is consistent with frequency-integrated TRTS data on FCPIB (see Supporting Information, Figure S6), as well as those from pure $FAPbI_3$ under 760-nm or 800-nm pump,[36] where the signal also shows a slow increase over the same timescale and similarly attributed to exciton dissociation. Note that the frequency-integrated TRTS signal consists of contributions from the carriers (*via* the DS term) and the phonons (*via* the PS term), which partially cancels each other. Thus the increase in the frequency-integrated signal with pump-probe time delay in Ref.[36] is not as large as that shown in Fig. 4A, which contains the carrier part only. It is fascinating that, even up to 3 ns, the free-carrier density is still increasing and shows no sign of decaying.

Pump-enhanced free-carrier screening

We now turn to another effect of carrier–phonon coupling on the photogenerated carriers, namely electrostatic screening of electron–hole pairs. The screening cloud surrounding the charge carriers efficiently renormalizes the bare Coulomb potential V_{bare} *via* the dielectric function $\tilde{\epsilon}(\omega, \tau)$.[37] The effective screened potential V_{eff} can be expressed as

$$V_{eff}(\omega, \tau) = \frac{V_{bare}}{\tilde{\epsilon}(\omega, \tau)}.$$

Figure 4C shows, at 15 and 285 K, the photoinduced enhancement of free-carrier screening factor $\mathrm{Re}(1/\tilde{\epsilon})$ at 0.5 THz, at different pump-probe time delays, normalized to the value before photoexcitation. At 15 K, though the screening is stronger at short time delays, it quickly recovers towards the equilibrium value, while at 285 K, the screening factor remains at a constant value of 80% (of the equilibrium value) up to 3 ns. The presence of screening reduces the exciton binding energy,[5] and thus further enhances exciton dissociation to free electrons and holes. Together with the results of the previous section, at room temperature, both electrostatic screening and exciton dissociation can now compete with carrier recombination, thus slowing down the decrease of carriers due to recombination and therefore maintaining a large free-carrier population over a long period of time.

A recent time-resolved photoluminescence and elastic neutron scattering study revealed a possible source of this screening in $FAPbI_3$ — the rotation of the organic cation $HC(NH_2)_2^+$ molecules in response to the presence of photogenerated charge carriers maximizes screening, resulting in a longer carrier lifetime than in $MAPbI_3$.[38]

Figure 4D summarizes the interplay among free carriers, excitons and low-lying phonon modes, based on our present work. Upon photoexcitation with a near-bandgap-energy photon, both free carriers and excitons are generated. Thermal energy provides these carriers with sufficient kinetic energy. Subsequently, a large number of hot phonons is generated *via* carrier cooling. These hot phonons can be reabsorbed by excitons, thus dissociating the

excitons to form free charge carriers. At the same time, Coulomb screening is enhanced due to the presence of photogenerated free charge carriers — this photoenhanced Coulomb screening results in a reduction of the exciton binding energy, which further facilitates the dissociation of excitons and creates even more free charge carriers. This combination of phonon-assisted exciton dissociation, carrier regeneration and enhanced carrier screening results in a positive feedback that ensures a long-lived free charge carrier population. This favorable circumstance is even more pronounced at room temperature — the large thermal energy of the carriers above the LO-phonon mode energies (see inset of Fig. 4A) ensures more carrier relaxation channels and phonon emission (by carriers). This in turn causes a long-lived (∼ns) phonon absorption process by excitons (Fig. 4B), resulting in enhanced exciton dissociation and therefore large carrier density (Fig. 4A). However, the low-energy phonon modes provide more scattering channels for the free charge carriers, reducing their carrier mobility, compared to systems with higher energy phonon modes (*e.g.* GaAs[30]). Note that the strong photoinduced change in the phonon modes and long rise in carrier population were only observed with an excitation at the band edge energy in FA-based perovskite family. They were not seen in non-FA-based perovskites, nor when the pump excitation energy is not at the gap edge.[6,36]

In our picture, the LO-phonons act as mediators between the free carriers and excitons, where phonon emission by carriers form excitons, while phonon absorption by excitons form free carriers. For this to happen, the LO-phonon energy must be similar to the binding energy of the excitons (which is true for the halide perovskite family), and these phonons must remain in the system for emission and reabsorption to continually take place. An alternative way of explaining this "oscillation" between the carrier and exciton densities is a coherent quantum superposition between the excitonic states and free carriers, neither of which are now an eigenstate due to coupling with phonons.

A previous transient absorption work[21] observed a very slow carrier cooling, and attributed it to the presence of a hot-phonon bottleneck upon photoexcitation with higher

energy photons. Subsequent works attribute the observed hot-phonon bottleneck to (1) the suppression of the Klemens relaxation pathway in $MAPbI_3$,[22] or (2) acoustic-optical phonon up-conversion that is especially strong in $FAPbI_3$ compared to $MAPbI_3$,[39] due to the overlapping phonon branches caused by the presence of the organic cations. Hence we can assume that the decay of optical to acoustic phonons is very weak, resulting in a long-lived optical (*i.e.* hot) phonon population. In our present work, due to the ability of TRTS to directly track the carrier density and phonon spectral weights, we found that the hot phonons contribute not only to slower carrier cooling, but also carrier generation *via* phonon-assisted exciton dissociation.

Conclusion

In summary, one of the distinguishing features of the Pb-halide semiconductor system is the presence of low-frequency phonon modes. These low-frequency modes reduce the carrier mobility *via* the introduction of more scattering pathways (emission and absorption) relative to semiconductors with higher-frequency modes, where only phonon emission is likely. There is a large population of phonons at room temperature (thus the 'liquid-like' nature of the system) that can help to reduce carrier trapping into shallow defects. It is also apparently easier to drive the phonon system out-of-equilibrium leading to slower carrier cooling. Here we show that time-resolved THz spectroscopy is ideally suited for studying electron–phonon interactions in the Pb-halide semiconductor system. TRTS can monitor both the carrier population as well as the low-frequency phonon modes immediately after photoexcitation, and thus is able to infer the interplay between the carrier, phononic and excitonic degrees of freedom. We show that, as expected, for a good semiconductor that the carriers and excitons relax *via* carrier-phonon interactions (phonon emission and absorption) establishing a thermal equilibrium between phonons, carriers and excitons. On one hand, excitons dissociate *via* phonon absorption to yield free carriers. On the other hand, excitons can form *via*

phonon emission from free carriers, thus reducing the free-carrier population. Our analysis directly resolves these interactions on the picosecond timescale.

Methods

Sample fabrication

Formamidinium iodide (FAI) was synthesized according to Ref.[12] The reagents were dissolved in ethanol and recrystallized at -3℃ overnight. Perovskite precursor solution $FA_{0.85}Cs_{0.15}Pb(I_{0.97}Br_{0.03})_3$ was prepared by dissolving FAI, CsI, PbI_2 and $PbBr_2$ with respective stoichiometric ratio in DMF/DMSO (4:1 v/v) at 80℃. *Z*-cut quartz substrates (10 mm × 10 mm × 1 mm) were cleaned thoroughly in Hellmanex II^{TM} solution (1% v/v), deionized water, acetone and isopropanol for 15 min each in an ultrasonic bath. Immediately before deposition of the photovoltaic precursor solution, the substrates were subjected to an air plasma treatment for 5 min and subsequently transferred to a nitrogen glove box. The perovskite solution (1 mol/L) was spin-coated on *z*-cut quartz at 1000 rpm for 10 s, and 4000 rpm for 30 s. 250 μL of chlorobenzene were dripped on the sample surface at 15 s of the second step spin-coating. Subsequently, the perovskite layer was annealed at 80℃ for 5 min, 120℃ for 5 min, and 180℃ for 30 min. The thickness of our final polycrystalline FCPIB film is 580 ± 20 nm. The sample is mounted in a cryostat with a cryocooler for cooling down to 15 K.

Time-resolved terahertz spectroscopy

The sample was excited by 790 ± 10 nm (1.57 ± 0.02 eV) optical pump pulses from a bandpass-limited output of an optical parametric amplifier set at 790 nm. The pump-probe time delay τ, between the near-infrared pump pulse and the terahertz (THz) pulse, and the THz time delay t, between the THz pulse and the gate pulse, are set by two motorized delays stages. THz pulses (with frequency range 0.5 THz to 2.3 THz) are generated in a 1 mm-thick ZnTe crystal through optical rectification, transmitted through the thin film,

and detected by electro-optical sampling in another ZnTe crystal. By modulating both the pump and probe beams, both the transmitted THz electric field $E(t,\tau)$ and its photoinduced change $\Delta E(t,\tau)$ are measured simultaneously at different pump-probe time delays τ (see Fig. 1A). At each pump-probe time delay τ, we scan the THz emitter delay in reverse, with pump and gate delays fixed. This synchronization procedure ensures that every part of the measured THz pulse experiences the same time delay from the pump pulse,[30] and enables sub-THz-wavelength detection. In this case, the time resolution of TRTS is only limited by the laser pulse duration in THz detection crystal (∼100 fs), rather than the THz pulse duration itself. For more details one can refer to the work by Beard *et al.*.[30] By use of an analytical expression of the transmission function of a film on a substrate without using any thin-film approximation, we extract the photoinduced change in the complex optical conductivity (or photoconductivity) $\Delta\tilde{\sigma}(\omega,\tau)$.[6,18] The photoconductivity contains both real $\Delta\sigma_1$ and imaginary $\Delta\sigma_2$ parts without requiring the use of the Kramers-Kronig transformation.

Supporting Information Available

Dielectric function and loss function analysis. LO-phonon mode consistency with the Cochran-Cowley relation. Carrier–phonon coupling constant calculation. J-V characteristics. Scanning electron microscopy images of FCPIB thin films. Temperature-dependent absorption spectra. Room-temperature photoluminescence. Phonon anharmonicity. Frequency-integrated TRTS. The combined photoconductivity model from phonon and carriers. Temperature-dependent THz conductivities of thin-film FCPIB.

This material is available free of charge *via* the Internet at http://pubs.acs.org/.

Acknowledgement

E.E.M.C. acknowledges support from the Singapore Ministry of Education AcRF Tier 2 (MOE2015-T2-2-065 and MOE2016-T2-1-054). C.L. is grateful to the supports from the Theoretical and Computational Science (TaCS) Center, Thailand Research Fund (MRG6080264) and KMUTT 55^{th} Anniversary Commemorative Fund. M.C.B. acknowledges funding from the Center for Hybrid Organic Inorganic Semiconductors for Energy (CHOISE) an Energy Frontier Research Center funded by the Office of Science of the US Department of Energy. Part of this work was authored in part by Alliance for Sustainable Energy, LLC, the manager and operator of the National Renewable Energy Laboratory for the U.S. Department of Eenrgy (ODE) under Contract No.DE-AC36-08GO28308. Y.M.L. acknowledges financial support from a Ministry of Education, Singapore, Tier 1 Funding (RG105/18). R.A.M. thanks the ONR and ARO for their support. M.-E.M.-B. is grateful to the Nanyang Technological University for supporting the Biophysics Center. The work was supported in part by the Center for Integrated Nanotechnologies, a U.S. DOE BES user facility.

References

1. Snaith, H. J. Perovskites: The Emergence of a New Era for Low-Cost, High-Efficiency Solar Cells. *J. Phys. Chem. Lett.* **2013**, *4*, 3623–3630.

2. Yin, W.-J.; Shi, T.; Yan, Y. Unique Properties of Halide Perovskites as Possible Origins of the Superior Solar Cell Performance. *Adv. Mater.* **2014**, *26*, 4653–4658.

3. Stranks, S. D.; Eperon, G. E.; Grancini, G.; Menelaou, C.; Alcocer, M. J. P.; Leijtens, T.; Herz, L. M.; Petrozza, A.; Snaith, H. J. Electron–Hole Diffusion Lengths Exceeding 1 Micrometer in an Organometal Trihalide Perovskite Absorber. *Science* **2013**, *342*, 341–344.

4. Xing, G.; Mathews, N.; Sun, S.; Lim, S. S.; Lam, Y. M.; Grätzel, M.; Mhaisalkar, S.;

Sum, T. C. Long-Range Balanced Electron- and Hole-Transport Lengths in Organic-Inorganic $CH_3NH_3PbI_3$. *Science* **2013**, *342*, 344–347.

5. Manser, J. S.; Kamat, P. V. Band Filling with Free Charge Carriers in Organometal Halide Perovskites. *Nat. Photon.* **2014**, *8*, 737–743.

6. La-o-vorakiat, C.; Salim, T.; Kadro, J.; Khuc, M. T.; Haselsberger, R.; Cheng, L.; Xia, H.; Gurzadyan, G. G.; Su, H.; Lam, Y. M.; Marcus, R. A.; Michel-Beyerle, M.-E.; Chia, E. E. M. Elucidating the Role of Disorder and Free-Carrier Recombination Kinetics in $CH_3NH_3PbI_3$ Perovskite Films. *Nat. Commun.* **2015**, *6*, 7903.

7. Wu, X.; Tan, L. Z.; Shen, X.; Hu, T.; Miyata, K.; Trinh, M. T.; Li, R.; Coffee, R.; Liu, S.; Egger, D. A.; Makasyuk, I.; Zheng, Q.; Fry, A.; Robinson, J. S.; Smith, M. D.; Guzelturk, B.; Karunadasa, H. I.; Wang, X.; Zhu, X.; Kronik, L. *et al.* Light-Induced Picosecond Rotational Disordering of the Inorganic Sublattice in Hybrid Perovskites. *Sci. Adv.* **2017**, *3*, e1602388.

8. Noh, J. H.; Im, S. H.; Heo, J. H.; Mandal, T. N.; Seok, S. I. Chemical Management for Colorful, Efficient, and Stable Inorganic–Organic Hybrid Nanostructured Solar Cells. *Nano Lett.* **2013**, *13*, 1764–1769.

9. Yang, J.; Siempelkamp, B. D.; Liu, D.; Kelly, T. L. Investigation of $CH_3NH_3PbI_3$ Degradation Rates and Mechanisms in Controlled Humidity Environments Using *In Situ* Techniques. *ACS Nano* **2015**, *9*, 1955–1963.

10. Lee, J.-W.; Kim, D.-H.; Kim, H.-S.; Seo, S.-W.; Cho, S. M.; Park, N.-G. Formamidinium and Cesium Hybridization for Photo- and Moisture-Stable Perovskite Solar Cell. *Adv. Energy Mater.* **2015**, *5*, 1501310.

11. Kulbak, M.; Gupta, S.; Kedem, N.; Levine, I.; Bendikov, T.; Hodes, G.; Cahen, D. Cesium Enhances Long-Term Stability of Lead Bromide Perovskite-Based Solar Cells. *J. Phys. Chem. Lett.* **2015**, *7*, 167–172.

12. Eperon, G. E.; Stranks, S. D.; Menelaou, C.; Johnston, M. B.; Herz, L. M.; Snaith, H. J. Formamidinium Lead Trihalide: A Broadly Tunable Perovskite for Efficient Planar Heterojunction Solar Cells. *Energy Environ. Sci.* **2014**, *7*, 982–988.

13. Yang, W. S.; Park, B.-W.; Jung, E. H.; Jeon, N. J.; Kim, Y. C.; Lee, D. U.; Shin, S. S.; Seo, J.; Kim, E. K.; Noh, J. H. Iodide Management in Formamidinium-Lead-Halide–Based Perovskite Layers for Efficient Solar Cells. *Science* **2017**, *356*, 1376–1379.

14. Ulbricht, R.; Hendry, E.; Shan, J.; Heinz, T. F.; Bonn, M. Carrier Dynamics in Semiconductors Studied with Time-Resolved Terahertz Spectroscopy. *Rev. Mod. Phys.* **2011**, *83*, 543–586.

15. Ahmed, T.; Salim, T.; Lam, Y. M.; Chia, E. E. M.; Zhu, J.-X. Optical Properties of Organometallic Perovskite: An *Ab Initio* Study Using Relativistic GW Correction and Bethe-Salpeter Equation. *Europhys. Lett.* **2015**, *108*, 67015.

16. La-o-vorakiat, C.; Xia, H.; Kadro, J.; Salim, T.; Zhao, D.; Ahmed, T.; Lam, Y. M.; Zhu, J.-X.; Marcus, R. A.; Michel-Beyerle, M.-E.; Chia, E. E. M. Phonon Mode Transformation Across the Orthohombic–Tetragonal Phase Transition in a Lead Iodide Perovskite $CH_3NH_3PbI_3$: A Terahertz Time-Domain Spectroscopy Approach. *J. Phys. Chem. Lett.* **2016**, *7*, 1–6.

17. Zhao, D.; Skelton, J. M.; Hu, H.; La-o-vorakiat, C.; Zhu, J.-X.; Marcus, R. A.; Michel-Beyerle, M.-E.; Lam, Y. M.; Walsh, A.; Chia, E. E. M. Low-Frequency Optical Phonon Modes and Carrier Mobility in the Halide Perovskite $CH_3NH_3PbBr_3$ Using Terahertz Time-Domain Spectroscopy. *Appl. Phys. Lett.* **2017**, *111*, 201903.

18. La-o-vorakiat, C.; Cheng, L.; Salim, T.; Marcus, R. A.; Michel-Beyerle, M.-E.; Lam, Y. M.; Chia, E. E. M. Phonon Features in Terahertz Photoconductivity Spectra Due to Data Analysis Artifact: A Case Study on Organometallic Halide Perovskites. *Appl. Phys. Lett.* **2017**, *110*, 123901.

19. Wehrenfennig, C.; Liu, M.; Snaith, H. J.; Johnston, M. B.; Herz, L. M. Charge-Carrier Dynamics in Vapour-Deposited Films of the Organolead Halide Perovskite $CH_3NH_3PbI_{3-x}Cl_x$. *Energy Environ. Sci.* **2014**, *7*, 2269–2275.

20. Yettapu, G. R.; Talukdar, D.; Sarkar, S.; Swarnkar, A.; Nag, A.; Ghosh, P.; Mandal, P. Terahertz Conductivity within Colloidal $CsPbBr_3$ Perovskite Nanocrystals: Remarkably High Carrier Mobilities and Large Diffusion Lengths. *Nano Lett.* **2016**, *16*, 4838–4848.

21. Yang, Y.; Ostrowski, D. P.; France, R. M.; Zhu, K.; van de Lagemaat, J.; Luther, J. M.; Beard, M. C. Observation of a Hot-Phonon Bottleneck in Lead-Iodide Perovskites. *Nat. Photon.* **2015**, *10*, 53–59.

22. Fu, J.; Xu, Q.; Han, G.; Wu, B.; Huan, C. H. A.; Leek, M. L.; Sum, T. C. Hot Carrier Cooling Mechanisms in Halide Perovskites. *Nat. Commun.* **2017**, *8*, 1300.

23. Wright, A. D.; Verdi, C.; Milot, R. L.; Eperon, G. E.; Pérez-Osorio, M. A.; Snaith, H. J.; Giustino, F.; Johnston, M. B.; Herz, L. M. Electron–Phonon Coupling in Hybrid Lead Halide Perovskites. *Nat. Commun.* **2016**, *7*, 11755.

24. Lloyd-Hughes, J.; Jeon, T.-I. A Review of the Terahertz Conductivity of Bulk and Nano-Materials. *J. Infrared Millim. Terahertz Waves* **2012**, *33*, 871–925.

25. Lowndes, R. P. Influence of Lattice Anharmonicity on the Longitudinal Optic Modes of Cubic Ionic Solids. *Phys. Rev. B* **1970**, *1*, 2754–2763.

26. Huber, R.; Kübler, C.; Tübel, S.; Leitenstorfer, A.; Vu, Q. T.; Haug, H.; Köhler, F.; Amann, M.-C. Femtosecond Formation of Coupled Phonon-Plasmon Modes in InP: Ultrabroadband THz Experiment and Quantum Kinetic Theory. *Phys. Rev. Lett.* **2005**, *94*, 027401.

27. Smith, N. V. Classical Generalization of the Drude Formula for the Optical Conductivity. *Phys. Rev. B* **2001**, *64*, 155106.

28. Cocker, T. L.; Baillie, D.; Buruma, M.; Titova, L. V.; Sydora, R. D.; Marsiglio, F.; Hegmann, F. A. Microscopic Origin of the Drude-Smith Model. *Phys. Rev. B* **2017**, *96*, 205439.

29. Whalley, L. D.; Skelton, J. M.; Frost, J. M.; Walsh, A. Phonon Anharmonicity, Lifetimes, and Thermal Transport in $CH_3NH_3PbI_3$ from Many-Body Perturbation Theory. *Phys. Rev. B* **2016**, *94*, 220301.

30. Beard, M. C.; Turner, G. M.; Schmuttenmaer, C. A. Transient Photoconductivity in GaAs as Measured by Time-Resolved Terahertz Spectroscopy. *Phys. Rev. B* **2000**, *62*, 15764–15777.

31. Amat, A.; Mosconi, E.; Ronca, E.; Quarti, C.; Umari, P.; Nazeeruddin, M. K.; Grätzel, M.; De Angelis, F. Cation-Induced Band-Gap Tuning in Organohalide Perovskites: Interplay of Spin–Orbit Coupling and Octahedra Tilting. *Nano Lett.* **2014**, *14*, 3608–3616.

32. Kasap, S., Capper, P., Eds. *Springer Handbook of Electronic and Photonic Materials*; Springer: New York, 2017.

33. Galkowski, K.; Mitioglu, A.; Miyata, A.; Plochocka, P.; Portugall, O.; Eperon, G. E.; Wang, J. T.-W.; Stergiopoulos, T.; Stranks, S. D.; Snaith, H. J. Determination of the Exciton Binding Energy and Effective Masses for Methylammonium and Formamidinium Lead Tri-Halide Perovskite Semiconductors. *Energy Environ. Sci.* **2016**, *9*, 962–970.

34. Luo, L.; Men, L.; Liu, Z.; Mudryk, Y.; Zhao, X.; Yao, Y.; Park, J. M.; Shinar, R.; Shinar, J.; Ho, K.-M.; Perakis, I. E.; Vela, J.; Wang, J. Ultrafast Terahertz Snapshots of Excitonic Rydberg States and Electronic Coherence in an Organometal Halide Perovskite. *Nat. Commun.* **2017**, *8*, 15565.

35. Ni, L.; Huynh, U.; Cheminal, A.; Thomas, T. H.; Shivanna, R.; Hinrichsen, T. F.; Ahmad, S.; Sadhanala, A.; Rao, A. Real-Time Observation of Exciton–Phonon Coupling

Dynamics in Self-Assembled Hybrid Perovskite Quantum Wells. *ACS Nano* **2017**, *11*, 10834–10843.

36. Piatkowski, P.; Cohen, B.; Ponseca Jr, C. S.; Salado, M.; Kazim, S.; Ahmad, S.; Sundström, V.; Douhal, A. Unraveling Charge Carriers Generation, Diffusion, and Recombination in Formamidinium Lead Triiodide Perovskite Polycrystalline Thin Film. *J. Phys. Chem. Lett.* **2016**, *7*, 204–210.

37. Huber, R.; Tauser, F.; Brodschelm, A.; Bichler, M.; Abstreiter, G.; Leitenstorfer, A. How Many-Particle Interactions Develop after Ultrafast Excitation of an Electron–Hole Plasma. *Nature* **2001**, *414*, 286–289.

38. Chen, T.; Chen, W.-L.; Foley, B. J.; Lee, J.; Ruff, J. P. C.; Ko, J. Y. P.; Brown, C. M.; Harriger, L. W.; Zhang, D.; Park, C.; Yoon, M.; Chang, Y.-M.; Choi, J. J.; Lee, S.-H. Origin of Long Lifetime of Band-Edge Charge Carriers in Organic–Inorganic Lead Iodide Perovskites. *Proc. Natl. Acad. Sci.* **2017**, *114*, 7519–7524.

39. Yang, J.; Wen, X.; Xia, H.; Sheng, R.; Ma, Q.; Kim, J.; Tapping, P.; Harada, T.; Kee, T. W.; Huang, F. Acoustic-Optical Phonon Up-Conversion and Hot-Phonon Bottleneck in Lead-Halide Perovskites. *Nat. Commun.* **2017**, *8*, 14120.

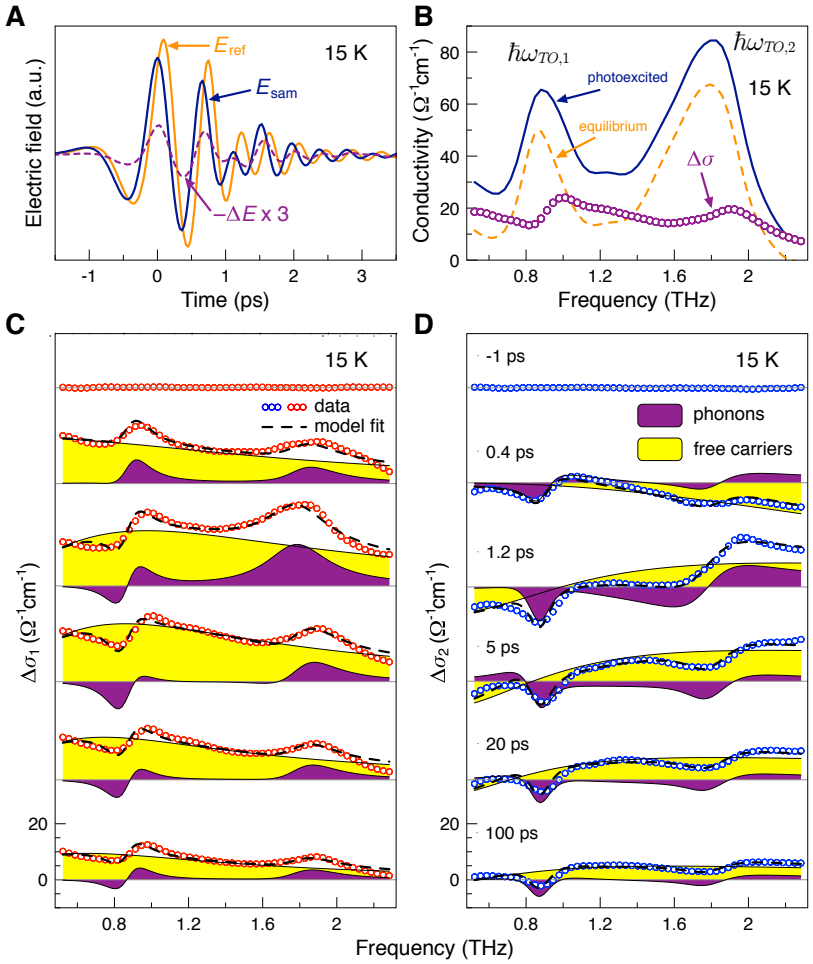

Figure 1: **Frequency-resolved photoconductivity spectra.** (A) THz time-domain data of the alloyed FA-perovskite $FA_{0.85}Cs_{0.15}Pb(I_{0.97}Br_{0.03})_3$ thin films after optically excitation with 790-nm pump pulses. The photoconductivity is calculated from the transmitted THz electric field through the perovskite film (E_{sam}), z-cut quartz reference (E_{ref}) and the photoinduced change (ΔE). (B) Real part of photoconductivity [$\Delta\sigma_1(\omega)$] (purple circles) obtained by the difference between the photoexcited (navy blue) and the equilibrium THz conductivity (orange). The two peaks show the approximate locations of the lowest-lying TO-phonon modes. The (C) real and (D) imaginary part of THz photoconductivity at different pump-probe delays, showing the contributions from Drude-Smith (DS, yellow area) and peak-shift (PS, purple area) terms. The DS term arises from photogenerated charge carriers in a disordered background, while the PS term accounts for the change in the oscillator strength and phonon resonant frequency.

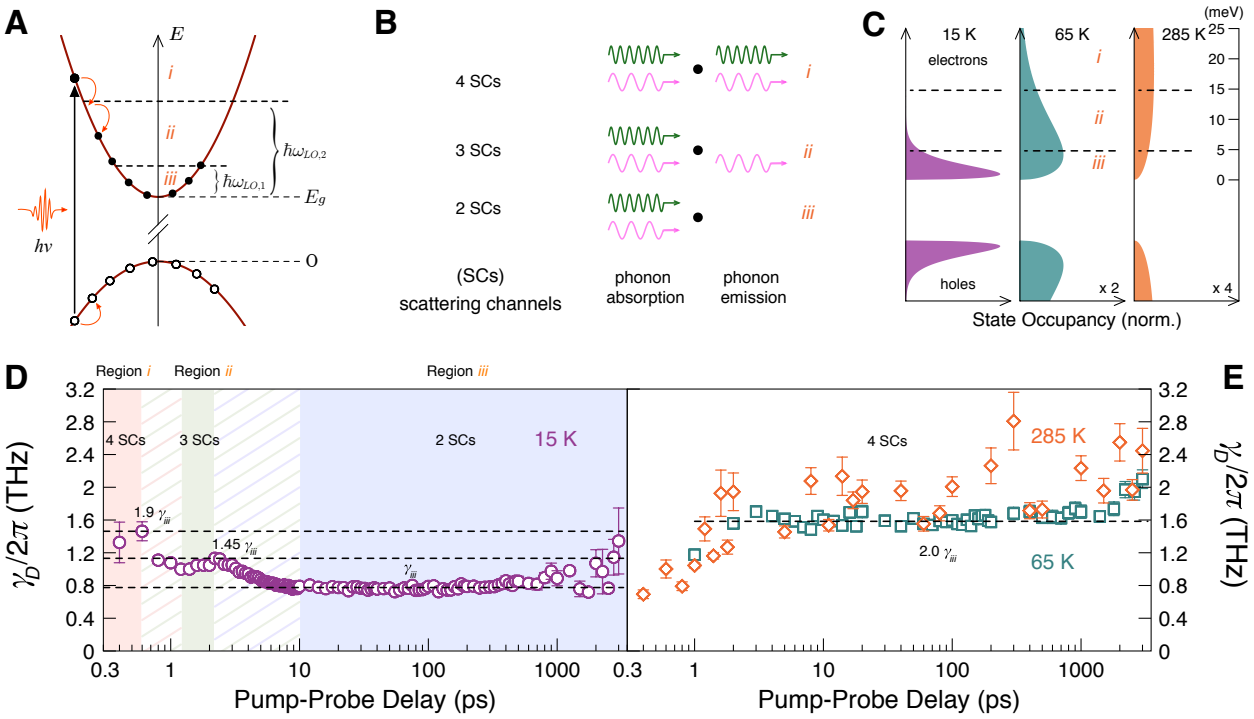

Figure 2: **Energy-dependent carrier relaxation channels.** (A) An optical excitation generates free electrons that relax from region *i* down towards *iii* delineated by phonon-mode energies $\hbar\omega_{LO,1}$ and $\hbar\omega_{LO,2}$. Only electrons with kinetic energy above the phonon mode energy can both absorb and emit a phonon; only phonon absorption can occur with lower kinetic energy. (B) The number of electron scattering channels reduces from 4 to 3 to 2, as the electrons relax from regions *i* to *ii* to *iii*. (C) Finite-temperature state occupancy calculated from the Fermi-Dirac distribution and density of states in a three-dimensional parabolic band, showing a temperature-dependent high-energy tail. State occupancies are normalized by the total carrier density. (D) Step-like transitions of carrier scattering rate (three horizontal dashed lines), obtained from the Drude-Smith model, in the ratio 3.8:2.9:2.0. This is close to the 4:3:2 ratio deduced from the number of scattering channels as the electrons relax towards the band edge going from region *i* to *ii* to *iii*. The larger error bars at very long time delays may be due to the small photoinduced signals. (E) With sufficient thermal energy at 65 K and 285 K, there is a significant fraction of carriers in region *i* (see Fig. 2C), opening up all four scattering channels. This results in the scattering rate at 65 K scaling closer to a factor of 4/2, and a slightly higher value at 285 K.

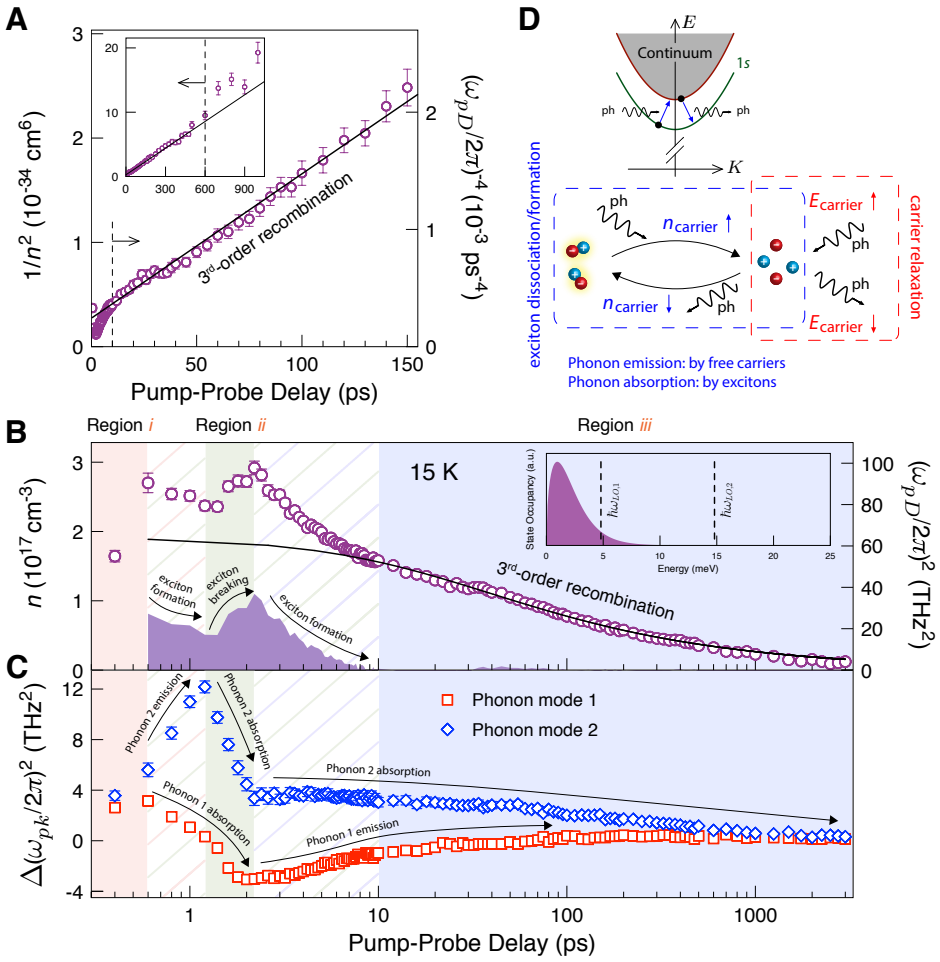

Figure 3: **Resolving the interplay between carrier and phonon spectral weights.** (A) The linear relationship between $1/n^2$ and pump-probe delay τ indicates predominantly third-order recombination, especially in the region between 10 ps to 600 ps. The deviation of the data from linearity below 10 ps suggests that carrier recombination is dominant after 10 ps, *i.e.* in region *iii* near the band edge (see Fig. 2A). (B) Time evolution of the photogenerated carrier density n at 15 K. Solid line is the third-order recombination curve plotted using the weighted-least-squares linear-fit parameters (between 10 and 600 ps) in Fig. 3A, then extrapolated down to 0.6 ps and up to 3000 ps. The difference between the experimental data and solid curve is indicated by the purple region. (C) Time evolution of the photoinduced change in spectral weight of phonon mode 1 (0.85 THz) and mode 2 (1.80 THz). By comparing Figs. 3B and 3C, one sees that in region *ii*, a decrease in the spectral weight of both phonon modes is accompanied by an increase in carrier density. This can happen only when phonons are absorbed by the excitons, thereby dissociating the excitons to become free carriers. In region *iii* where the carriers are already near the band edge, phonon emission and absorption slows down, and (third-order) recombination is now dominant. (D) Schematic showing phonon-related mechanisms that affect carrier density and carrier energy. Top figure depicts the excitation spectrum of electron-hole pairs with energy E and center-of-mass momentum K, and the processes of exciton dissociation (formation) accompanied by phonon absorption (emission) by excitons (free carriers). Only the $1s$ excitonic level is shown for clarity.

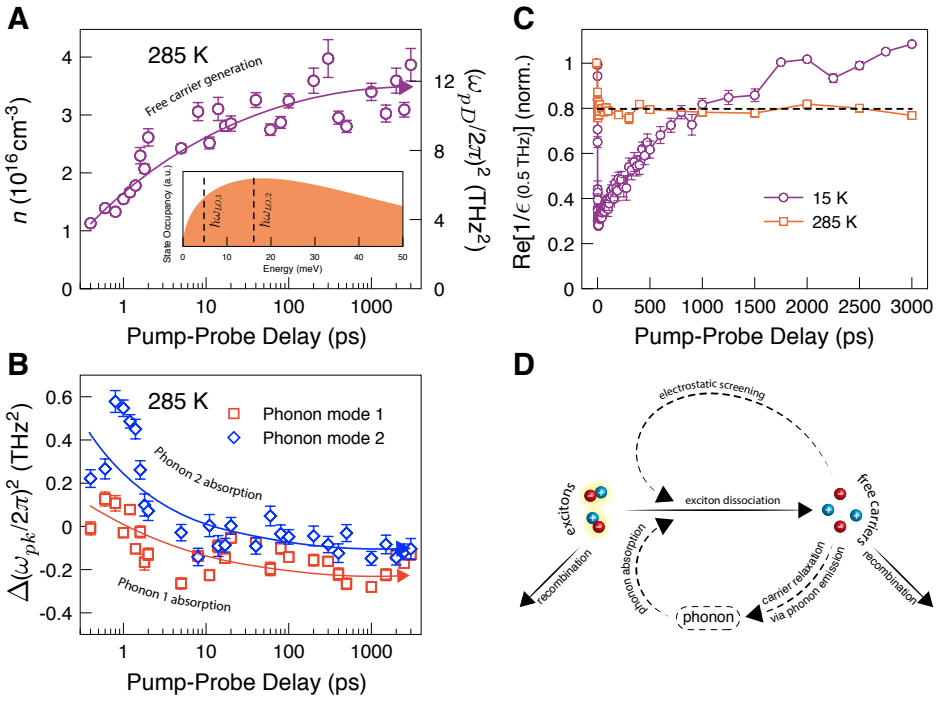

Figure 4: **Room-temperature spectral weight evolution and photoenhanced free-carrier screening.** Time-resolved spectral weight change of (A) free carriers, (B) phonon mode 1 (0.85 THz) and mode 2 (1.80 THz) at 285 K. (C) Electrostatic (or Coulomb) screening factor Re$(1/\tilde{\epsilon})$ at 0.5 THz as a function of pump-probe delay, at 15 K and 285 K. Note the long-lived screening factor of 0.8 at 285 K even up to 3 ns. (D) A schematic showing the dissociation of excitons *via* the interplay with free carriers, electrostatic screening and low-lying phonons to maintain a large and long-lived free-carrier population in the system.

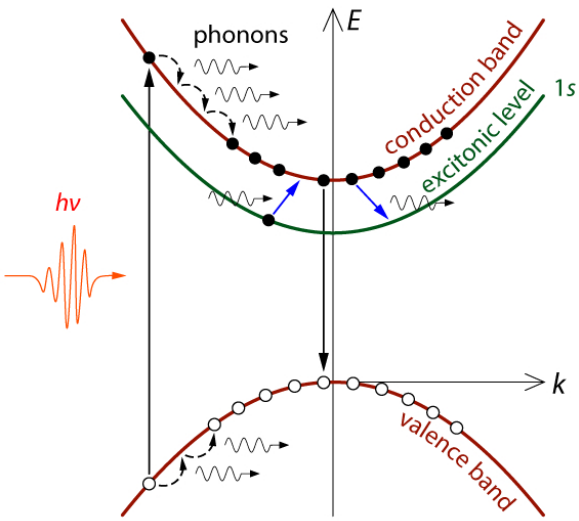
phonons
E
conduction band
1s
excitonic level
hν
k
valence band